11
Fluid–Fluid and Fluid–Solid Mass Transfer*

Michiel T. Kreutzer and Axel Günther

11.1
Introduction

This chapter provides an overview of the mass transfer characteristics of multiphase microreactors. Basic concepts are explained and related to mass transfer in sequented (drop/bubble) flow, annular flow, and to multiphase flow through packed microchannels. In multiphase microreactors, a chemical reaction can either involve two immiscible fluid phases (e.g. for gas–liquid reactions) or two fluid phases in the presence of a solid catalyst or the reaction is exclusively confined to one of the fluid phases that are present in the system.

11.1.1
Relevance

Several recent reviews have been published on multiphase microreactors [1–4]. In large-scale equipment, the rate of mass transfer from one phase to the other is often slow with respect to the considered reaction rate, a phenomenon that leads to significant mass transfer limitations. Because of the excellent heat and mass transfer characteristics associated with multiphase microreactors, such reactions are good candidates for being conduced at the microscale [5–7]. It should be emphasized, however, that miniaturization *per se* does not improve mass transfer rates. Many macroscopic reactors are turbulent: the exchange of matter associated with turbulent eddies can be very fast, depending on the turbulence intensity. In microfluidic and microreactor systems that are characterized by viscous flows in the absence of turbulence, such secondary flow patterns are generally lacking and diffusion in laminar liquid flows is notoriously slow.

Molecules that participate in a chemical reaction often need to travel from a chemically inert phase to the reacting phase. In addition, the inert phase can serve as a sink that removes molecules from the reacting phase and it is also possible that an

*A List of Symbols can be found at the end of this chapter.

Micro Process Engineering, Vol.1: Fundamentals, Operations and Catalysts
Edited by V. Hessel, A. Renken, J.C. Schouten, and J.-I. Yoshida
Copyright © 2009 WILEY-VCH Verlag GmbH & Co. KGaA, Weinheim
ISBN: 978-3-527-31550-5

inert phase is not involved in the chemical reaction at all, but only serves to enhance mixing between two miscible fluids [8, 9]. Microfluidic networks that do not contain any phase partaking in a chemical reaction, except exclusively passive (inert) ones, can be used to facilitate unit mass transfer operations at the microscale. Examples are extraction or post-reaction separation [10–16]. Microscale multiphase systems can further be classified according to whether they contain mobile phases, typically fluids, and/or stationary phases, typically solids that are catalytically active. In fact, many multiphase system contain, apart from a moving fluid, only a heterogeneous catalyst [17, 18]. The simplest case consists of a single stationary phase with a single mobile phase. More complex cases include two immiscible fluid streams with a chemical reaction taking place in one of them [19], such as fluorinations [20, 21] and aminocarbonylations [22], and three-phase systems, where two fluid phases carry molecules that participate in the chemical reaction and the third solid phase acts as a catalyst [7, 23]. We should also stress that a number of microscale systems purposefully take advantage of the slow mass transfer rates in the absence of any convection. Mass transfer enhancement across a fluid interface is therefore not always the objective. In fact, droplet trains where each droplet serves as an isolated reactor achieve minimal cross-talk [24, 25].

11.1.2 Basics, Relevant Time Scales

In the considered cases, transport of matter occurs by diffusion and by convection. The characteristic diffusion time is given by $t_D = L^2/D$, indicating that molecules initially confined to a single spot spread in space over a distance that is proportional to the square root of time. Although microfluidic systems are small, with length scales in the range $10^{-4} < L < 10^{-5}$ m, diffusion times can nevertheless be significant in liquids with diffusivities of $10^{-9} < D < 10^{-12}\,m^2\,s^{-1}$. The large variation in values of D reflects the large spread in molecule size, from fast-diffusion molecules such as H_2 to slower diffusing larger molecules, such as proteins, DNA fragments and nanoparticles. Also, interphase boundaries can extend over the entire length of the reactor or alternatively span a distance smaller than the hydraulic diameter of a microchannel. The characteristic time scale for convection is given by $t_C = L/U$, which also varies significantly in microreactors, because of the different velocities needed to accommodate the wide range of reaction times needed for different chemistries. The ratio of the diffusion time and the convection time is the dimensionless Péclet number, $Pe = UL/D$.

From a balance on a differential control volume, the species reaction–convection–diffusion equation for a first-order reacting system is given by

$$\frac{\partial C}{\partial t} + U\nabla C = D\Delta C - k_R C \tag{11.1}$$

where C is the species concentration. We can write this equation for each of the phases, where the convective term $U\nabla C$ vanishes if stationary phases are considered and the reaction term $k_R C$ vanishes for inert phases. The boundaries of each phase are described by impermeable walls, for which there can be no gradient dC/dn in the wall-normal direction or by an interfacial boundary, where at the interface an equilibrium concentration $C_{(a)} = mC_{(b)}$ is reached. The dimensionless constant m

is a thermodynamic parameter dependent on temperature and pressure. These boundary conditions are linear in concentration, as is Equation (11.1) for a first-order reaction. The entire dynamics of the interplay of reaction, diffusion and convection are independent of the absolute concentration level, which is a convenient result.

To explore the relative importance of the different terms in Equation (11.1), we rescale all variables such that the concentration and its derivatives, distances and times are all of order one. The concentration is normalized using the highest expected concentration in the system, typically that of the main reactant in the feed stream. We normalize time using the convection time, i.e. $\theta = U/Lt$, and the Cartesian coordinates using length scale L, i.e. $x^* = x/L$, etc. In a dimensionless form we write

$$\frac{\partial C}{\partial \theta} + \nabla C = Pe^{-1}\Delta C - Da^{-1}C \tag{11.2}$$

where Pe denotes the previously defined Péclet number. The Damköhler number, $\mathrm{Da} = U/k_R L$, is defined as the ratio of the reaction time to the convection time. We distinguish two steady-state cases of a reacting phase:

1. *The Damköhler number is very large with respect to the Péclet number.* If this is the case, then the reaction is so slow that concentration gradients even out to equilibrium values. This is the situation that is desired when one is interested in measuring the rate of a chemical reaction, because all the concentrations are uniformly defined by equilibrium ratios. This condition can be rewritten into the following well-known result in heterogeneous catalysis:

$$\frac{Da}{Pe} = \frac{D}{k_R L^2} >> 1 \text{ or } L\sqrt{\frac{k_R}{D}} < 1 \tag{11.3}$$

   where the group $L(\mathrm{k_R}/D)^{1/2}$ is known in the field of catalysis as the Thiele modulus. In the context of gas–liquid reactions, the same group is often referred to as the Hatta number.

2. *The Damköhler number is very small with respect to the Péclet number.* Now, all the reactant will be consumed immediately and a thin concentration boundary layer develops close to interphase boundaries that supply fresh reactants.

In the non-reacting case, we can also distinguish two very similar cases: at small values of the Péclet number, the concentration gradients are quickly equilibrated by diffusion, whereas for large values of the Péclet number, convection dominates.

The scaling analysis presented so far applies for laminar, well-behaved flows where all the relevant characteristic times can be estimated to determine whether mass transfer limitations occur. Full solutions for the convection–diffusion-reaction problem, however, are difficult to obtain analytically for all but the simplest flow problems.

A simple case that can be solved analytically is the so-called Graetz problem, in which mass transfer to the wall of a straight channel is calculated for the entry region of a microchannel where an infinitely fast reaction occurs at the wall. This problem, depicted in Figure 11.1, is representative for many aspects of laminar-flow mass transfer in microfluidic systems and heterogeneous microreactor applications, so we discuss it in some detail.

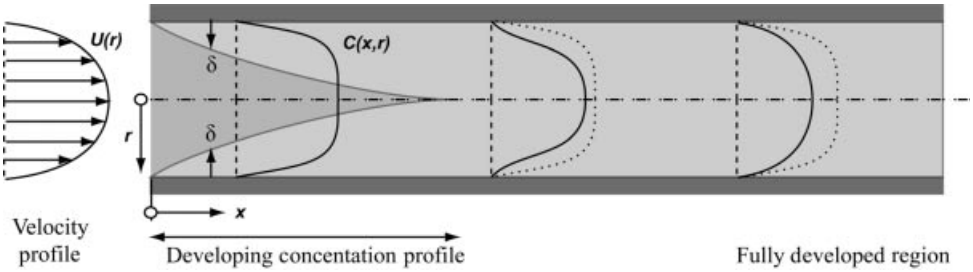

Figure 11.1 The Graetz problem for forced convection in a microchannel (diameter d_h) with developed laminar flow. The gray profiles indicate the streamwise development of the concentration profile. The concentration profile near the entrance is unaffected by the fast first-order reaction at the wall. Outside this region, the concentration profile is still flat. The thickness of the concentration boundary layer is indicated by δ. Further downstream, a developed region that is characterized by a self-similar concentration profile is obtained (the original profile is shown as a dotted line for comparison).

At the inlet of the channel, the velocity profile is well developed and the concentration profile is uniform, giving rise to an infinitely high mass transfer rate. Further downstream, a boundary layer of thickness δ develops that grows with the streamwise coordinate. The rate of mass transfer to the wall, per unit area is given by Fick's law:

$$J = D\frac{\mathrm{d}C}{\mathrm{d}n} \tag{11.4}$$

where n is the coordinate normal to the surface of the wall. The mass transfer coefficient k is defined as the ratio of the flux and the concentration gradient. The order of magnitude of the flux is then given by $J \sim (D/\delta)\Delta C$, so $k \sim D/\delta$. In correlations, the mass transfer coefficient is usually reported as the dimensionless Sherwood number:

$$Sh = \frac{kL}{D} \tag{11.5}$$

Approximately at a distance $x/d \sim Pe$ downstream, the boundary layer has extended to the center of the microchannel. With the mass transfer coefficient $k \sim D/d_h$, we can estimate $Sh \approx 1$. Exact calculations show that the developed value is $Sh = 3.66$ for round channels. In the entry region, the scaling $Sh \sim (x/d_h Pe)^{-1/3}$ applies – a result that was obtained by Graetz and by Nusselt in the nineteenth century. The mathematical details of the derivation are reported in most mass transfer textbooks. The monograph by Shah and London [26] contains detailed calculations for many channel geometries, including those that are regularly found in microfluidic channels, such as rectangular cross-sections. A discussion of numerical solutions of the Graetz problem is given in [27].

For many microfluidic applications, especially in multiphase flow, the situation is much more complex than the Graetz problem, but the concept of boundary layers and associated mass transfer coefficients is generally a useful one. In the absence of flow, the thickness of a developing boundary layer can be estimated by $\delta(t) \sim (Dt)^{1/2}$. For flowing systems, one can often follow a fluid element during contact with another phase and estimate the mass transfer parameter as $k \sim D/\delta(t) = (D/t)^{1/2}$, where t indicates the time during which the fluid element remains at the interface. This approach is called

penetration theory [28]. Sometimes a boundary layer of constant thickness δ_0 develops and an estimate $k \sim D/\delta_0$ is derived by applying a *film theory* [29] based approach.

We now move from the differential balance equation for a given species [Equations (11.1) and (11.2)] to an integral equation. One of the phases of a multiphase fluid system is considered. If the phase is confined to a volume V with an interfacial area A that is available for exchange with a second phase, a balance of reaction and mass transfer gives

$$Vk_{\mathrm{R}}C = kA(C - C^*) \tag{11.6}$$

where C^* corresponds to the equilibrium concentration with the other phase. The group kA/V or ka with a specific surface area a is obtained by dividing Equation (11.6) by the volume and has the unit time^{-1}. The characteristic mass transfer time is $(ka)^{-1}$. Note that many experimental methods measure the product ka, rather than k or a separately. In macroscopic equipment, it is nearly impossible to separate the two, but many of the regular microfluidic flow patterns allow the specific surface area to be quantified from micrographs.

The Sherwood number $Sh = kL/D$ can be regarded as the ratio of the diffusion time in the absence of flow, L^2/D, to the actual mass transfer time, $1/ka$ ($\sim L/k$). In the following sections of this chapter, we discuss various fluid–fluid microreactor configurations and discuss how mass transfer rates in them may be predicted using penetration theory and film theory. In the following paragraph, we briefly discuss experimental methods to determine mass transfer rates.

Mass transfer rates can be measured using a variety of methods. One can distinguish reactive methods and non-reactive methods. With non-reactive methods, two phases that are far from equilibrium are exposed to one another. The change in concentration typically behaves as an exponential decay and the rate of change can be related to the group ka. The mass transfer rate that is obtained by non-reactive methods is the lower limit for a given hydrodynamic situation. When a reaction occurs in the system, mass transfer is enhanced. One can regard mass transfer and reaction as resistances in series. With increasing reaction rates, mass transfer becomes the limiting resistance. Reactive mass transfer experiments are used to determine this upper limit. Reaction rates increase sharply with temperature, whereas mass transfer is nearly independent of temperature. A practical way to find the upper limit is therefore to increase the temperature until the reactor performance becomes independent of temperature. The reaction rate that is observed at that point corresponds to the maximum mass transfer rate. Or, in different words, the maximum mass transfer rate is obtained at the temperature where the apparent activation energy drops to zero (practically, the limit is $E_{\mathrm{A,obs}} < 8\,\mathrm{kJ\,mol^{-1}}$).

11.2
Stable Fluid Interfaces: Annular Flows and Falling Films

In many multiphase microreactor applications, stable fluid interfaces have been particularly important for performing gas–liquid reactions in the annular flow

regime. We assume the liquid to be perfectly wetting and to form a stable film of thickness δ_F at all microchannel walls. The gas phase fills the core of the channel. An example is direct fluorination that has been realized in microreactors under annular and segmented flow conditions [30–32]. Annular flow microreactors have been fabricated in different materials, including silicon, nickel and stainless steel. One of the first configurations that provided vertical downflow of the gas and liquid phases is the so-called "falling film reactor" [33].

At given gas and liquid superficial velocities j_G and j_L that are defined by the volumetric flow rate of the respective phase divided by the cross-sectional area of the microchannel, de Mas *et al.* [30] solved the force balance for the two co-flowing fluid phases. A capillary with a diameter equal to the hydraulic diameter of the microreactor was considered (Figure 11.2). The annular flow was assumed to be axisymmetric, laminar and fully developed. Using a constant pressure gradient in the gas and liquid phases along the streamwise direction, the flow satisfies the equations

$$-\frac{\mathrm{d}P}{\mathrm{d}x}+\rho_G g+\mu_G\frac{1}{r}\frac{\mathrm{d}}{\mathrm{d}r}\left(r\frac{\mathrm{d}U_{x,G}}{\mathrm{d}r}\right)=0\ (\text{gas}) \tag{11.7}$$

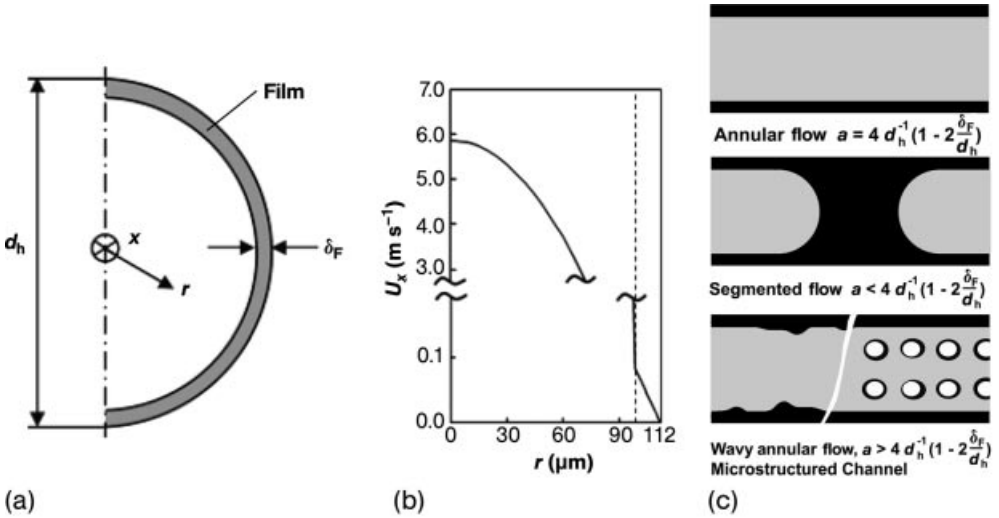

Figure 11.2 Film distribution for annular flow through a microchannel that is represented by a cylindrical capillary of diameter d_h with circular cross-section. (a) de Mas *et al.* [30] calculated the film thickness and velocity distributions. Schematic cross-sectional configuration with the gas flow through the center and a uniformly distributed film wetting the walls. Two parallel microchannels was represented by capillaries of hydraulic diameter 224 μm for flows of 5 cm^3 min^{-1} for nitrogen (G) and 22.5 μL min^{-1} for acetonitrile (L) per tube. (b) The velocity distribution obtained in the gas core and liquid film is shown as a function of the radial distance. The location of the gas–liquid interface is indicated as a dashed line. (c) Specific surface area *a* in annular (film) flow and segmented flow and opportunities for increased surface areas in wavy annular flows and flows through microstructured packings.

$$-\frac{dP}{dx}+\rho_L g+\mu_L\frac{1}{r}\frac{d}{dr}\left(r\frac{dU_{x,L}}{dr}\right)=0\ (\text{liquid}) \tag{11.8}$$

with the boundary conditions

$$\left.\begin{aligned}U_{x,L}(R)&=0\\ \frac{dU_{x,G}}{dr}(0)&=0\end{aligned}\right\}\ (\text{wall})\qquad \left.\begin{aligned}U_{x,l}(\delta_F)&=U_{x,g}(\delta_F)\\ \mu L_l\frac{dU_{x,L}}{dr}(\delta_F)&=\mu_G\frac{dU_{x,G}}{dr}(\delta_F)\end{aligned}\right\}\ (\text{interface}) \tag{11.9}$$

where P, μ, g, U_x, δ_F and R are the pressure, fluid viscosity, gravitational acceleration, axial velocity, radial position of the gas–liquid interface and radius of the capillary, respectively. The subscripts G and L indicate gas and liquid phases, respectively. A simple analytical solution exists [34] and expressions for the gas and liquid volumetric flow rates were obtained by integrating the velocities over the appropriate cross-sectional area. For a flow rate of $5\,cm^3\,min^{-1}$ of nitrogen and $22.5\,\mu L\,min^{-1}$ of acetonitrile flowing horizontally and evenly distributed through a representative tube, de Mas *et al.* [30] estimated the liquid film to be 14 μm thick with a pressure drop of 860 Pa for a 2-cm-long channel. The calculated gas and liquid velocity profiles are shown in Figure 11.2.

Note that the assumption of a circular cross-section is a simplification for most microfabricated reactors since rectangular or triangular cross-sections generally prevail in microfluidic channel networks that are patterned by using lithography and bulk silicon/glass/metal machining techniques. In contrast to a circumferentially homogeneous film thickness δ_F that we assumed previously, microchannel corners are filled with liquid menisci.

In many cases, annular flows correspond to conditions of very high superficial gas velocities, often on the order of $1\,m\,s^{-1}$, and relatively low superficial liquid velocities. The interfacial area A between the gas and the liquid phase is equal to $\pi(d_h-2\delta_F)$. Hence the specific surface area for annular flows is $a=4d_h^{-1}\left(1-2\delta_F d_h^{-1}\right)$ (Figure 11.2c). At sufficiently high superficial velocities, the fluid interface becomes wavy, a flow regime that is sometimes referred to as "wavy-annular" flow. The effect increases the interfacial area and likely enhances mass transfer within the liquid film. Another strategy for increasing the specific surface area that we will come back to in Section 11.4 is to fill the microreaction channel with packings of either stationary microparticles or microfabricated posts.

11.3
Droplet/Bubble Segmented Flows

A second important flow pattern for conducting chemical reactions is segmented flow. In such flows, segments of a disperse phase extend over almost the entire microchannel cross section $\sim d_h$. Dispersed fluid segments can be either droplets or bubbles. Although we focus on bubbles in this section, most of the analysis is directly

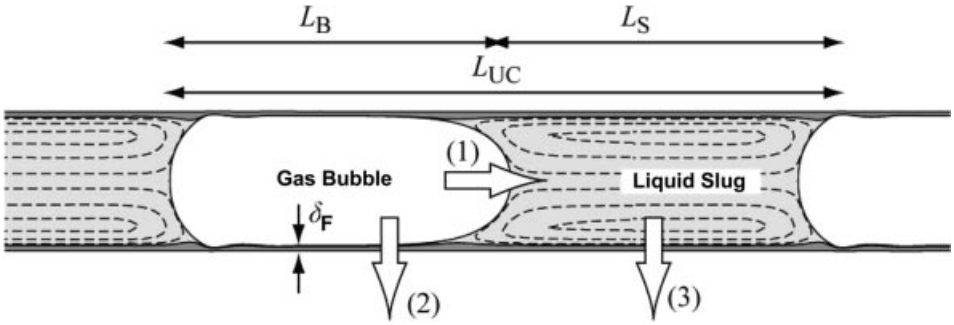

Figure 11.3 Different mass transfer mechanisms in gas–liquid segmented flow (Taylor flow): (1) from the bubble to the recirculation region in a liquid segment (slug), (2) between a bubble and the microchannel wall and (3) from the recirculating liquid region to the microchannel wall. Note that the third step may consist of a convective–diffusive contribution within the recirculation region and a pure diffusive contribution in the film region.

applicable also to liquid–liquid systems. Between neighboring bubbles, the continuous phase forms liquid segments or *slugs*. We assume that the continuous phase perfectly wets the microchannel wall. The flow pattern is shown schematically in Figure 11.3. For a study of the mass transfer behavior, we briefly discuss the main characteristics of fluid flow in the continuous phase. Inside a slug, the liquid forms a "caterpillar" circulating motion (in a reference frame moving along with the bubble). The wetting liquid forms a thin lubricating layer between the disperse segments and the wall, which is indicated in dark gray in Figure 11.3. This lubricating layer remains at the wall when the recirculating region passes by. Liquid in this layer does not mix with the liquid in the recirculating region. As a result, mass transfer between the two regions occurs by diffusion only.

We identify several relevant length scales in the system: the thickness of the lubricating layer δ_F, the length of the discrete segment or bubble $L_B \sim L_F$ and the length of the slug L_S. We abbreviate the length of a unit cell containing one bubble and one slug as L_{UC}. These lengths all depend on mechanisms related to the formation of the segmented flow [35, 36] and lubrication theory [37] and will be treated as known quantities here.

A complete understanding of all the mass transfer steps requires us to consider (1) $k_{GL}a_{GL}$, the mass transfer from a bubble to the continuous liquid, (2) $k_{GW}a_{GW}$, the mass transfer from a gas bubble directly to the solid wall, and (3) $k_{LW}a_{LW}$, the mass transfer from the continuous liquid in the recirculating region to the solid wall. How all of these mass transfer steps interact depends strongly on the boundary conditions at the wall. If no reaction occurs on the wall, then the lubricating film acts as a capacitor for transfer from the bubble to the slug by dissolving molecules from the bubble and releasing them by diffusion into the recirculating region. Transfer through the lubricating layer can add significantly to the direct transfer from the bubble to the slug at the bubble caps. On the other hand, when dissolved gases are consumed by a fast reaction at the wall, the concentration at the wall approaches zero

and the lubricating film will never be saturated. In this case, bubble-to-slug transfer occurs exclusively at the caps.

Because the mechanism of mass transfer changes so significantly when a reaction takes place, it is dangerous to measure gas-to-liquid mass transfer and liquid-to-solid mass transfer independently and then combine them for gas-to-liquid-to-solid $(ka)_{GLW}$ as resistances in series according to

$$(ka)_{GLW} = k_{GW}a_{GW} + \left(\frac{1}{k_{GL}a_{GL}} + \frac{1}{k_{LW}a_{LW}}\right)^{-1} \tag{11.10}$$

The use of resistances in series in Equation (11.10) is valid only when $k_{GL}a_{GL}$ refers to transfer at the caps only.

11.3.1 Fluid–Fluid Mass Transfer Without Reaction at the Wall

In this section, we analyze the case of zero reaction at the wall in detail. The time needed to saturate the lubricating layer by diffusion is of the order $t_F \sim \delta_F{}^2/D$. We can compare this time with the time it takes a bubble or a liquid slug to pass over this layer, $t_B \sim L_B/U$ and $t_S \sim L_S/U$, respectively. If the passing time for the bubbles is much greater than the film saturation time, $t_B > t_F$, then the lubricating film is saturated with dissolved gases each time a bubble passes by. Similarly, when $t_S > t_F$, the lubricating film will equilibrate completely with the concentration of dissolved gas in the recirculating region.

Seminal work on segmented flow mass transfer was conducted by Higbie [38], who used experiments at $t_B < t_F$ to prove the now well-established but then new penetration theory, i.e. that $k_L \sim (D/t_B)^{1/2}$. More recently, Irandoust *et al.* [39] modeled gas absorption in segmented (Taylor) flow. They assumed a penetration theory for the film between the bubble and the wall and found agreement with experiment with limited adjustable curve-fitting parameters.

Bercic and Pintar [40] measured gas–liquid mass transfer in a single channel for a wide range of superficial gas and liquid velocities (Figure 11.4). Their experimental set-up allowed the independent variation of bubble and slug length, but most of their experiments were performed under conditions where $t_B > t_F$. They correlated their data for a methane-water system as

$$k_L a = \frac{0.111\,U^{1.19}}{L_S^{0.57}} \tag{11.11}$$

Interestingly, the mass transfer from Equation (11.11) is a function of the slug length and hardly a function of the bubble length. The explanation is that the lubricating film near the wall is completely saturated each time the bubble passes by, such that increasing the bubble length does not improve mass transfer. It is then safe to conclude that Equation (11.11) describes (1) the partial depletion of the film between the wall and the slug as the slug passes by and (2) the transfer of gas to the

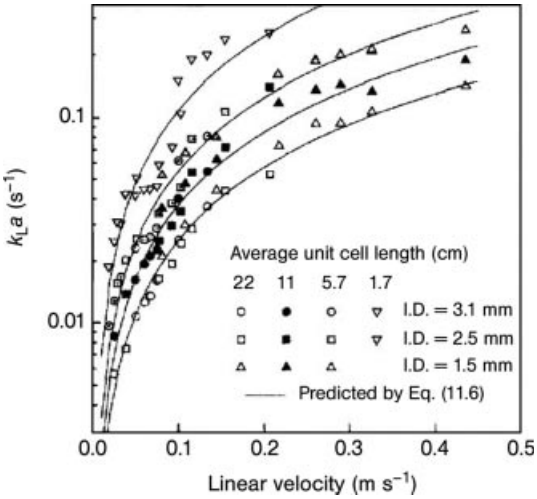

Figure 11.4 Influence of the velocity and unit cell length, i.e. the sum of bubble and slug length, on measured k_La coefficients at fixed gas hold-up. From [40].

slug at the bubble caps. The specific interfacial area associated with transfer from the caps is independent of channel diameter. Bercic and Pintar varied the channel diameter between 1.5 and 3.1 mm and found no impact of channel diameter, which suggests that transfer from the caps is important.

Van Baten and Krishna [41] performed a computational fluid dynamics (CFD) study of gas absorption in Taylor flow and found that in some of the experiments of Bercic and Pintar the contact time in the film was indeed long enough to saturate the liquid film fully. For shorter unit cells (or higher velocities), they formulated a mass transfer model of penetration theory for both the caps and the film

$$(k_La)_{caps} = \frac{8\sqrt{2}}{\pi L_{UC}}\sqrt{\frac{DU}{d_h}} \tag{11.12}$$

$$k_{L,F} = \begin{cases} 2\sqrt{\dfrac{D}{\pi t_F}}\dfrac{\ln(1/\Phi)}{1-\Phi} (Fo<0.1) \\ 3.41\dfrac{D}{\delta_F} (Fo>1) \end{cases} \tag{11.13}$$

$$a_F = \frac{4L_F}{dL_{UC}} \tag{11.14}$$

in which the Fourier number Fo and the parameter Φ are defined by

$$Fo = \frac{Dt_F}{\delta_F^2}, \quad \text{and estimate} \quad t_F \approx \frac{L_F}{U} \tag{11.15}$$

$$\Phi = 0.7857\exp(-5.212Fo) + 0.1001\exp(-39.21Fo) + \ldots \tag{11.16}$$

Note that for short contact times, the mass transfer group is a function of the channel diameter. In the majority of the simulations performed by van Baten and Krishna, the slugs were significantly longer than the bubbles, so depletion of the film in the slug region is likely. For gas absorption without reaction (at the wall or in the liquid), the alternating exposure of the lubricating film to bubbles and slugs periodically fills and empties this film and the relative length of the bubbles and slugs determines which has the most impact. This explains why different engineering correlations are found, some based on slug length, but others based on bubble length: the experimental range of bubble and slug lengths determines which correlation best fits the data and extrapolation of such correlations beyond the experimental bubble and slug contact times must be treated with caution.

11.3.2
Continuous Phase to Wall Mass Transfer

Now consider the transfer of a liquid phase component to a catalyst on the wall, where the component is reacted very rapidly. The best approach would be to consider two different mass transfer steps, one from the circulating region to the film, in series with a second film resistance inside the film. The first step can be considered by eliminating the film from consideration in a numerical study, while experimentally the film resistance can be eliminated by working under conditions where the lubricating layer has a negligible thickness. The principal features of the first mass transfer step can then be studied by ignoring the thin film and simplifying the gas–liquid interface to flat ends.

Duda and Vrentas [42] used this approach and found an infinite-series analytical solution for the closed-streamline axisymmetric flow in this cylinder. In a second paper [43], the corresponding developing heat transfer problem was solved using a formal Fourier series technique. The method allowed the calculation of time-dependent Nusselt numbers up to $L_S/d_h = 2.5$ for Péclet numbers of up to 400. Extension to higher L/d_h was prohibited as the eigenvalues of the solution became too close together as the aspect ratio was increased.

Analogous to the single-phase Graetz problem, the Graetz number $Gz = x/d_h Pe$ can be introduced (note that different definitions of the Graetz number are used in the literature). Kreutzer calculated the liquid–solid mass transfer in this simplified geometry with a finite-element method [44], arriving at different values to those reported in [43]. Kreutzer reported an expression for the length-averaged mass transfer from the recirculating region to the wall, without a lubricating film in between:

$$Sh = \sqrt{\alpha^2 + \frac{\beta}{Gz}} \tag{11.17}$$

with α and β being weak functions of the slug length L_S:

$$\alpha = 40\left[1 + 0.28\left(\frac{L_S}{d_h}\right)^{-4/3}\right] \tag{11.18}$$

$$\beta = 90 + 104\left(\frac{L_S}{d_h}\right)^{-4/3} \tag{11.19}$$

Equation (11.17) is defined per unit slug volume and should be multiplied by the liquid holdup to obtain a mass transfer coefficient based on microchannel volume. Also, this equation is only valid for the region in which the circulating region has circulated at least once. Before a full circulation, the effect of circulation has hardly manifested itself and the Sherwood numbers for very short tubes are complex non-monotonic functions of slug length and tube length.

Closer inspection of Equation (11.17) shows that even for long slugs, the asymptotic value for $Gz \rightarrow \infty$ is 40, which may be compared with 3.66 for the analogous single-phase case. Therefore, we can increase the liquid–solid mass transfer per unit liquid volume by a factor of 10 by adding gas bubbles to the system. Gruber and Melin [45] performed a numerical study of liquid–solid mass transfer in Taylor flow and studied mass transfer experimentally by dissolving a copper capillary in sulfuric acid–potassium dichromate solution. They considered the entire unit cell in their analysis and found that the film resistance could be ignored if $\delta_F/d_h < 0.01$. In a numerical study, van Baten and Krishna [46] used $\delta_F/d_h = 0.0016$ for simulations comprising a complete unit cell, including the bubble. Their results could be correlated as

$$Sh = 0.5\left(\frac{\varepsilon_G}{Gz}\right)^{0.15} Gz^{-\alpha} \tag{11.20}$$

where ε_G is the gas volume fraction and $\alpha \approx 0.48$ is a weak function of the slug length L_S.

Limited experimental data for liquid–solid mass transfer are available. Oliver and Hoon [47] measured heat transfer in two-phase flow in capillaries using very viscous liquids and hence with thick lubricating layers. The best data set is by Horvath *et al.* [48], who measured the hydrolysis of *N*-benzoylarginine ethyl ester in a 1.2 m long tube coated with the immobilized enzyme trypsin. The intrinsic rate of this reaction was high enough that mass transfer from the liquid was limiting. The experimental data are reported as *Sh* versus L_S/d_h with the Reynolds number *Re* as a parameter and *Sh* versus *Re* with the aspect ratio L_S/d_h as a parameter.

In Figure 11.5, the experimental data are compared with the results of Kreutzer [44]. The agreement of the cylindrical cavity calculations is very good for low Reynolds numbers, $U\rho d_h/\mu$. At higher Reynolds numbers, the impact of the film resistance increases and numerical predictions deviate from the experimental results for longer slugs.

11.3.3 Disperse Phase to Wall Mass Transfer

Now we consider the case of mass transfer from the bubble to a catalyst that is deposited at the wall of the microreactor channel, at which a dissolved gas is converted rapidly.

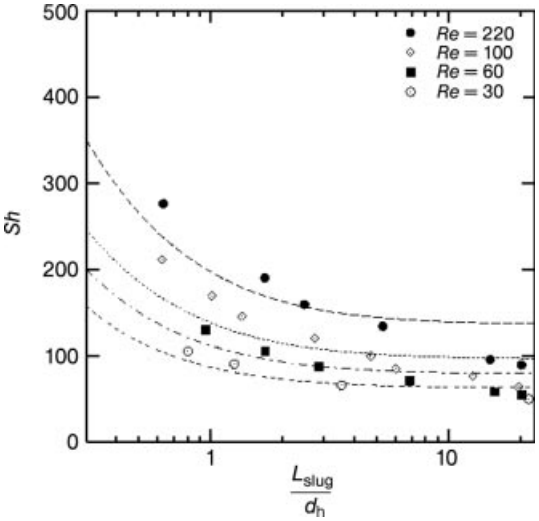

Figure 11.5 Sherwood number plotted against the slug aspect ratio. Experimental data from [48], lines based on Equation (11.17). Note that the applicability of Equation (11.17) is based on a negligible resistance in the lubricating film, which is satisfied here only for low *Re*.

For the liquid in the recirculating region, the transfer of gas that is dissolved at the caps is, at the steady state, equal to the transfer of dissolved gas to the wall. Figure 11.6 shows a typical flow simulation for a heterogeneously catalyzed hydrogenation reaction. For these conditions, the largest resistance to mass transfer in the slug is located in the thin-film region and the majority of the circulation zone is characterized by a region of constant concentration. Also, the slug is almost saturated and $C_S \approx C^*$.

The rate of transfer to the wall may be estimated from film theory as $k = D/\delta_F$ for a given film thickness δ_F. We assume here that δ is the same within the slug, i.e. the liquid layer close to the wall is not partaking in the recirculation and the bubble, and obtain

$$k_{BW} = \frac{D}{\delta_{BW}} \approx \frac{D}{\delta_{SW}} = k_{SW} \tag{11.21}$$

Figure 11.6 Mass transfer in segmented gas–liquid flow. Concentration contours for 20 equally spaced intervals between 0 and C^* are shown in the top half and streamlines are shown in the bottom half for a simulation with $D = 1.4 \times 10^{-8}\,m^2\,s^{-1}$, $U = 0.4\,m\,s^{-1}$, $d = 1.0\,mm$, $L_S + L_B = 4d_h$ and liquid volume fraction $\varepsilon = 0.5$ [44].

For the bubble region, the mass transfer rate can be estimated from film theory:

$$J_{GW} = kA(C^* - 0) = \frac{D}{\delta_F}\frac{4L_B}{d_h}(C^* - 0) \tag{11.22}$$

In the slug region, the same approach can be used, with the concentration in the circulating zone the following mass transfer rats is obtained:

$$J_{LW} = kA(C_S - 0) = \frac{D}{\delta_F}\frac{4L_B}{d_h}(C_S - 0) \tag{11.23}$$

The problem of formulating a mass transfer model can now be reduced to the problem of formulating a model that predicts the average slug concentration. Using penetration theory for the caps, it can be shown that

$$\frac{L_S}{\delta_F}\sqrt{\frac{D\pi}{8Ud_h}} = \frac{C^* - C_S}{C_S} \tag{11.24}$$

An important finding that is consistently reported in the literature is explained by CFD simulations: the impact of holdup is limited. If a liquid slug is completely saturated with the gas-phase component and if the film thickness can be assumed to be the same for the slug and the bubble, mass transfer is indeed completely independent of the holdup.

Figure 11.7 shows another important aspect of mass transfer to the wall in microreactor or monolith applications: the external mass transfer improves with decreasing velocity. This implies that the mass transfer increases with a decrease in pressure drop. This behavior is related to the fact that δ decreases when U decreases and is very different from intuitively expected behavior. The notion that enhancement

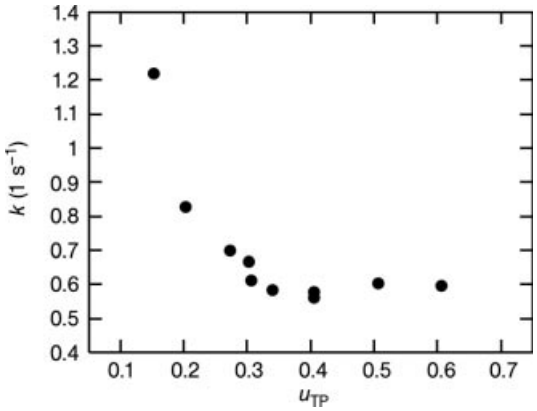

Figure 11.7 Observed pseudo-first-order reaction rate constant for hydrogenation in a monolith pilot reactor. The reaction was not completely mass transfer limited, but external mass transfer limitation did strongly affect the observed rate: for these experiments, $k_{obs,H_2} \approx k_{GLW}/2$. Note that the reaction rate decreases with decreasing throughput [44].

of mass transfer comes at the cost of an increase in pressure drop is almost an axiom in reactor engineering. It should be realized that such analogies are based on the dominance of eddy transport in turbulent flows and the behavior of the segmented flow in microchannels is by no means in contradiction with such analogies. The excellent mass transfer at minimal power input is one of the most useful features of multiphase microchannel, allowing an escape from the all too common trade-off of pressure drop and mass transfer.

11.4
Complex Geometries – Packed Beds and Foams

So far, we have considered catalytic materials that conform to the side walls of a microreactor. A downside to a functionalized coating at a channel wall is the limited catalytic surface area that can be provided. As an alternative, thin-film technology can be used for depositing catalytic materials on more complex three-dimensional surfaces inside microchannels [49]. Impregnation methods can also be used on porous silicon surfaces [50]. The mass transfer rates described for such structures are sufficient for all but the fastest heterogeneous reactions.

Mass transfer behavior can be improved significantly by microfabricating a high surface area secondary structure inside the microchannels. Designs featuring rows of high-aspect ratio pillars that were fabricated by deep reactive ion etching were reported for chromatographic applications [51, 52]. Such micropillar chromatographs have very limited band dispersion and good mixing properties – the plate heights are of the order of the spacing of the pillars. Alternatively, a fine powder of the heterogeneous catalysts can be introduced into the channel [7, 53]. Such packed beds have a much less regular packing, leading to flow irregularities. The advantage of this approach is that the microreactor can be periodically refilled with new catalysts and that any catalyst can be used, milled and sieved to the appropriate size.

Precise experimental measurements of mass transfer rates in such systems are still rare. Losey *et al* [50] microfabricated a packed-bed structure (Figure 11.8) in which they estimated the mass transfer rate by performing the fast cyclohexene hydrogenation

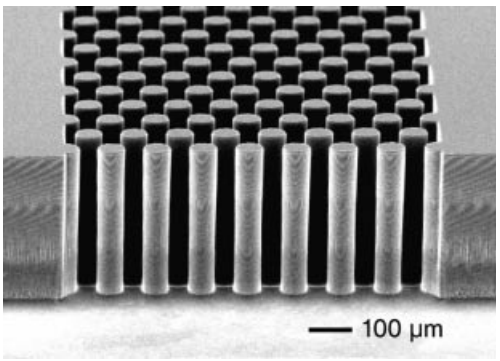

Figure 11.8 Micropillars of porous material that can be impregnated with catalyst. From [50].

reaction. They reported mass transfer rates ka in excess of 5–15 s^{-1}. However, activation energies were not reported and it is possible that mass transfer rates were even higher. For a packed bed with particle size d_p, a crude estimate is obtained using $k \sim D/d_p$ and $a \sim 1/d_p$. For a hydrogenation ($D \approx 10^{-9}$ m^2 s^{-1}) in a packed bed with 10^{-5} m particles, this predicts that ka is of the order 10 s^{-1}. The linear velocity in such reactors is of the order of 1 mm s^{-1}. Using penetration theory for a contact time $t = d_p/U$ then predicts ka of 10^2 s^{-1}. In comparison, for conventional macroscopic packed beds the maximum mass transfer rates are below 10^{-2} s^{-1}. In other words, micropacked beds can have three orders of magnitude higher productivity on a volumetric (or catalyst weight) basis. It should be noted that very few catalysts are active enough to push micropacked beds into the fully mass transfer limited regime.

Wada *et al.* [54] used a micropillar system with 50 µm pillars for a gas–liquid reaction that was mass-transfer limited, and estimated ka using ozonolysis reactions at 2.5 s^{-1}, which was five times higher than the transfer rate in a similar reactor without posts. In such a configuration, the posts break up the gas–liquid flow in the channel and increase the area for interphase mass transfer.

List of Symbols

A	Surface area available for mass transfer (m^2)
a	Specific surface area $= A/V$ (m^{-1})
C	Molar concentration (mol L^{-1})
C^*	Equilibrium concentration (mol L^{-1})
d_h	Hydraulic diameter (m)
d_p	Particle diameter (m)
D	Diffusivity (m^2 s^{-1})
E_A	Activation energy (J mol^{-1})
g	Gravitational acceleration (m s^{-2})
j_G	Superficial velocity of gas phase (m^2 s^{-1})
j_L	Superficial velocity of liquid phase (m^2 s^{-1})
J	Mass transfer rate
k_{GL}	Mass transfer coefficient, gas–liquid (m s^{-1})
k_{GW}	Mass transfer coefficient, gas–solid (m s^{-1})
k_{GLW}	Mass transfer coefficient, gas–liquid–solid overall (m s^{-1})
k_R	Rate of first-order chemical reaction (s^{-1})
L	Length scale (m)
L_B	Bubble length in flow direction $= L_F$ (m)
L_S	Slug length in flow direction (m)
L_{UC}	Length of a unit cell $= L_B + L_S$ (m)
m	Dimensionless constant
n	Coordinate in wall-normal direction (m)
P	Pressure (Pa)
r	Coordinate in radial direction (m)
R	Tube radius (m)

t	Time scale (s)
t_F	Time needed to saturate film by diffusion (s)
t_B	Time needed for bubble to advance by L_B in streamwise direction (s)
t_C	Convection time scale $= L/U$ (s)
U	Velocity ($m\,s^{-1}$)
V	Volume (m^3)
x	Cartesian (streamwise) coordinate (m)
y	Cartesian coordinate (m)
z	Cartesian coordinate (m)
δ	Thickness of concentration boundary layer (m)
δ_F	Liquid film thickness (m)
δ_0	Constant mass transfer boundary layer thickness obtained from film theory (m)
μ	Absolute viscosity (Pa s)
ρ	Fluid density ($kg\,m^{-3}$)
Θ	Dimensionless convection time

Dimensionless Groups

Da	Damköhler number ($Uk_R{}^{-1}L^{-1}$)
Fo	Fourier number ($Dt_F\delta_F{}^{-2}$)
Gz	Graetz number ($xd^{-1}Pe^{-1}$)
Pe	Péclet number (ULD^{-1})
Sh	Sherwood number (kLD^{-1})

References

1 G. N. Doku, *et al.,* On-microchip multiphase chemistry – a review of microreactor design principles and reagent contacting modes, *Tetrahedron*, **2005**, *61*, 2733–2742.

2 V. Hessel, *et al.,* Gas–liquid and gas–liquid–solid microstructured reactors: Contacting principles and applications, *Industrial and Engineering Chemistry Research*, **2005**, *44*, 9750–9769.

3 L. Kiwi-Minsker, A. Renken, Microstructured reactors for catalytic reactions, *Catalysis Today*, **2005**, *110*, 2–14.

4 M. T. Kreutzer, *et al.,* Multiphase monolith reactors: chemical reaction engineering of segmented flow in microchannels, *Chemical Engineering Science*, **2005**, *60*, 5895–5916.

5 J. R. Burns, C. Ramshaw, The intensification of rapid reactions in multiphase systems using slug flow in capillaries, *Lab on a Chip*, **2001**, *1*, 10–15.

6 M. T. Kreutzer, *et al.,* Mass transfer characteristics of three-phase monolith reactors, *Chemical Engineering Science*, **2001**, *56*, 6015–6023.

7 M. W. Losey, M. A. Schmidt, K. F. Jensen, Microfabricated multiphase packed-bed reactors: characterization of mass transfer and reactions, *Industrial and Engineering Chemistry Research*, **2001**, *40*, 2555–2562.

8 B. K. H. Yen, *et al.,* A microfabricated gas–liquid segmented flow reactor for high-temperature synthesis: the case of

CdSe quantum dots, *Angewandte Chemie International Edition*, **2005**, *44*, 5447–5451.

9 S. A. Khan, K. F. Jensen, Microfluidic synthesis of titania shells on colloidal silica, *Advanced Materials*, **2007**, *19*, 2556.

10 S. H. Cypes, J. R. Engstrom, Analysis of a toluene stripping process: a comparison between a microfabricated stripping column and a conventional packed tower, *Chemical Engineering Journal*, **2004**, *101*, 49–56.

11 Y. He, H. K. Lee, Liquid phase microextraction in a single drop of organic solvent by using a conventional microsyringe, *Analytical Chemistry*, **1997**, *69*, 4634–4640.

12 J. G. Kralj, H. R. Sahoo, K. F. Jensen, Integrated continuous microfluidic liquid-liquid extraction, *Lab on a Chip*, **2007**, *7*, 256–263.

13 H. R. Sahoo, J. G. Kralj, K. F. Jensen, Multistep continuous-flow microchemical synthesis involving multiple reactions and separations, *Angewandte Chemie International Edition*, **2007**, *46*, 5704–5708.

14 B. S. Broyles, S. C. Jacobson, J. M. Ramsey, Sample filtration, concentration and separation integrated on microfluidic devices, *Analytical Chemistry*, **2003**, *75*, 2761–2767.

15 R. D. Oleschuk, *et al.*, Trapping of bead-based reagents within microfluidic systems: on-chip solid-phase extraction and electrochromatography, *Analytical Chemistry*, **2000**, *72*, 585–590.

16 E. A. Schilling, A. E. Kamholz, P. Yager, Cell lysis and protein extraction in a microfluidic device with detection by a fluorogenic enzyme assay, *Analytical Chemistry*, **2002**, *74*, 1798–1804.

17 A. R. Bogdan, *et al.*, Improving solid-supported catalyst productivity by using simplified packed-bed microreactors, *Angewandte Chemie-International Edition*, **2007**, *46*, 1698–1701.

18 I. R. Baxendale, *et al.*, A flow process for the multi-step synthesis of the alkaloid natural product oxomaritidine: a new paradigm for molecular assembly, *Chemical Communications*, **2006**, 2566–2568.

19 C. de Bellefon, *et al.*, Microreactors for dynamic, high throughput screening of fluid/liquid molecular catalysis, *Angewandte Chemie International Edition*, **2000**, *39*, 3442–3445.

20 K. Jänisch, *et al.*, Chemistry in microstructured reactors, *Angewandte Chemie International Edition*, **2004**, *43*, 406–446.

21 N. de Mas, *et al.*, Microfabricated multiphase reactors for the selective direct fluorination of aromatics, *Industrial and Engineering Chemistry Research*, **2003**, *42*, 698–710.

22 E. R. Murphy, *et al.*, Accelerating reactions with microreactors at elevated temperatures and pressures: profiling aminocarbonylation reactions, *Angewandte Chemie-International Edition*, **2007**, *46*, 1734–1737.

23 J. Kobayashi, *et al.*, A microfluidic device for conducting gas-liquid-solid hydrogenation reactions, *Science*, **2004**, *304*, 1305–1308.

24 M. T. Kreutzer, A. Günther, K. F. Jensen, Sample dispersion for segmented flow in microchannels with rectangular cross section, *Analytical Chemistry*, **2008**, *80*, 1558–1567.

25 H. Song, D. L. Chen, R. F. Ismagilov, Reactions in droplets in microfluidic channels, *Angewandte Chemie International Edition*, **2006**, *45*, 7336–7356.

26 R. K. Shah, A. L. London, *Laminar Flow Forced Convection in Ducts. A Source Book for Compact Heat Exchanger Analytical Data*. Advances in Heat Transfer, Supplement 1, Academic Press, New York, **1978**.

27 W. E. Schiesser, C. A. Silebi, *Computational Transport Phenomena: Numerical Methods for the Solution of Transport Problems*, Cambridge University Press, Cambridge, **1997**.

28 R. Higbie, The rate of absorption of a pure gas into a still liquid during a short time of exposure, *Transactions of the American*

Institute of Chemial Engineers, **1935**, *31*, 365–389.

29 W. Nernst, Theorie der Reaktionsgeschwindigkeit in heterogenen Systemen, *Zeitschrift für Physikalische Chemie*, **1904**, *47*, 52–55.

30 N. de Mas, *et al.*, Scalable microfabricated reactors for direct fluorination reactions. In *Proceedings of IEEE Transducers*, Boston, **2003**.

31 N. de Mas, *et al.*, Scaled-out multilayer gas–liquid microreactor with integrated velocimetry sensors, *Industrial and Engineering Chemistry Research*, **2005**, *44*, 8997–9013.

32 K. Jaehnisch, *et al.*, Direct fluorination of toluene using elemental fluorine in gas/liquid microreactors, *Journal of Fluorine Chemistry*, **2000**, *105*, 117–128.

33 A. Gavriilidis, *et al.*, Technology and applications of microengineered reactors, *Chemical Engineering Research and Design*, **2002**, *80* (A1) 3–30.

34 C. E. Hickox, Instability due to viscosity and density stratification in axisymmetric pipe flow, *Physics of Fluids*, **1971**, *14*, 251.

35 P. Garstecki, *et al.*, Formation of droplets and bubbles in a microfluidic T-junction – scaling and mechanism of break-up, *Lab on a Chip*, **2006**, *6*, 437–446.

36 V. van Steijn, M. T. Kreutzer, C. R. Kleijn, mu-PIV study of the formation of segmented flow in microfluidic T-junctions, *Chemical Engineering Science*, **2007**, *620*, 7505–7514.

37 F. Bretherton, The motion of long bubbles in tubes, *Journal of Fluid Mechanics*, **1961**, *10*, 166–188.

38 R. Higbie, The rate of adsorption of pure gas into a still liquid during short periods of exposure, *Transactions of the American Institute of Chemical Engineers*, **1935**, *31*, 365–389.

39 S. Irandoust, S. Ertle, B. Andersson, Gas–liquid mass-transfer in Taylor flow through a capillary, *Canadian Journal of Chemical Engineering*, **1992**, *70*, 115–119.

40 G. Bercic, A. Pintar, The role of gas bubbles and liquid slug lengths on mass transport in the Taylor flow through capillaries, *Chemical Engineering Science*, **1997**, *52*, 3709–3719.

41 J. M. van Baten, R. Krishna, CFD simulations of mass transfer from Taylor bubbles rising in circular capillaries, *Chemical Engineering Science*, **2004**, *59*, 2535–2545.

42 J. L. Duda, J. S. Vrentas, Steady flow in region of closed streamlines in a cylindrical cavity, *Journal of Fluid Mechanics*, **1971**, *45*, 247.

43 J. L. Duda, J. S. Vrentas, Heat transfer in a cylindrical cavity, *Journal of Fluid Mechanics*, **1971**, *45*, 261.

44 M. T. Kreutzer,Hydrodynamics of Taylor flow in capillaries and monolith reactors. PhD Thesis, Delft University of Technology, **2003**.

45 R. Gruber, T. Melin, Radial mass transfer enhancement in bubble-train flow, *International Journal of Heat and Mass Transfer*, **2003**, *46*, 2799–2808.

46 J. M. van Baten, R. Krishna, CFD simulations of wall mass transfer for Taylor flow in circular capillaries, *Chemical Engineering Science*, **2005**, *60*, 1117–1126.

47 D. R. Oliver, A. Y. Hoon, Two-phase non-Newtonian flow. 2. Heat transfer, *Transactions of the Institution of Chemical Engineers and the Chemical Engineer*, **1968**, *46*, T116.

48 C. Horvath, B. A. Solomon, J. M. Engasser, Measurement of radial transport in slug flow using enzyme tubes, *Industrial and Engineering Chemistry Fundamentals*, **1973**, *12*, 431–439.

49 A. Iles, *et al.*, A simple technique for microfluidic heterogeneous catalytic hydrogenation reactor fabrication, *Catalysis Letters*, **2007**, *114*, 71–74.

50 M. W. Losey, *et al.*, Design and fabrication of microfluidic devices for multiphase mixing and reaction, *Journal of Microelectromechanical Systems*, **2002**, *11*, 709–717.

51 M. De Pra, *et al.*, Pillar-structured microchannels for on-chip liquid chromatography: evaluation of the permeability and separation performance,

Journal of Separation Science, **2007**, *30*, 1453–1460.

52 M. De Pra, *et al.*, Experimental study on band dispersion in channels structured with micropillars, *Analytical Chemistry*, **2006**, *78*, 6519–6525.

53 R. Abdallah, *et al.*, Gas-liquid and gas–liquid–solid catalysis in a mesh microreactor, *Chemical Communications*, **2004**, 372–373.

54 Y. Wada, M. A. Schmidt, K. F. Jensen, Flow distribution and ozonolysis in gas–liquid multichannel microreactors, *Industrial and Engineering Chemistry Research*, **2006**, *45*, 8036–8042.